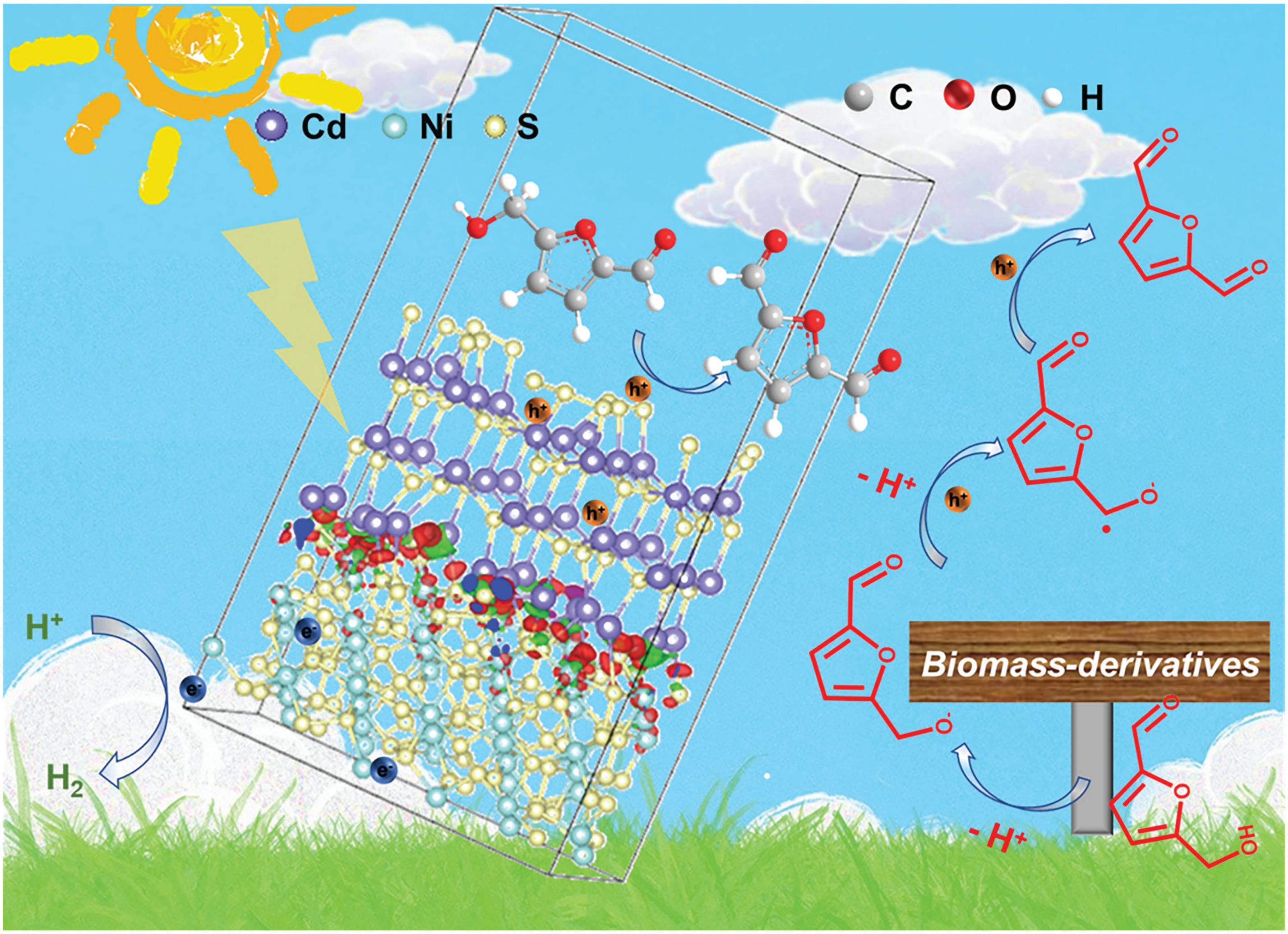

**Showcasing research from Professor Tiancheng Mu's laboratory, Renmin University of China, and Professor Zhimin Xue, Beijing Forestry University, Beijing, China.**

Deep eutectic solvothermal $NiS_2$/CdS synthesis for the visible-light-driven valorization of the biomass intermediate 5-hydroxymethylfurfural (HMF) integrated with $H_2$ production

CdS nanospheres deposited with $NiS_2$ was prepared by one-step deep eutectic solvothermal method. The prepared $NiS_2$/CdS exhibits efficiently visible-light-driven dehydrogenation of biomass intermediate 5-hydroxymethylfurfural (HMF) to one of the most important platform molecules in the organic chemicals industry 2,5-diformylfuran (DFF). The entire photocatalytic process could be achieved in water at ambient condition without using sacrificial agents or organic solvents. The photocatalytic dehydrogenation strategy could be used in other biomass-derivative transformation processes.

## As featured in:

See Zhimin Xue *et al.*, *Green Chem.*, 2023, **25**, 2620.

Green Chemistry

ROYAL SOCIETY OF CHEMISTRY

PAPER

View Article Online
View Journal | View Issue

Check for updates

**Cite this:** *Green Chem.*, 2023, **25**, 2620

# Deep eutectic solvothermal $NiS_2$/CdS synthesis for the visible-light-driven valorization of the biomass intermediate 5-hydroxymethylfurfural (HMF) integrated with $H_2$ production†

Shuzi Liu,[a] Baolong Zhang,[a] Zhaohui Yang,[a] Zhimin Xue *[b] and Tiancheng Mu *[a]

Received 29th November 2022,
Accepted 1st January 2023

DOI: 10.1039/d2gc04535d

rsc.li/greenchem

Visible-light-driven transformation of biomass to high-valued chemicals is attractive for achieving a low-carbon environment. The solar-catalyzed oxidation of 5-hydroxymethylfurfural (HMF) to 2,5-diformylfuran (DFF) has great industrial potential because DFF is a pivotal precursor in industries. Here, we present a one-step deep eutectic solvothermal technique for the production of $NiS_2$/CdS nanospheres. Because $NiS_2$ can act as a cocatalyst enhancing the transfer and separation of photogenerated carriers, the prepared $NiS_2$/CdS exhibits efficient visible-light-driven dehydrogenation of HMF to $H_2$ and DFF. DFF and $H_2$ can be produced at rates of up to 519.64 and 476.60 μmol $g^{-1}$ $h^{-1}$, respectively, which are about 10.03 and 9.81 times higher than those of bare CdS under visible light irradiation. Moreover, the photocatalytic process was carried out at ambient temperature and pressure in water without using a sacrificial agent. Both $h^+$ and $e^-$ are involved in the process of photocatalytic reaction, and the valence band position of the $NiS_2$/CdS photocatalyst is essential for the high DFF selectivity (95.2%). This work paves a sustainable way to realize the photocatalytic valorization of biomass.

## Introduction

5-Hydroxymethylfurfural (HMF) is one of the most promising chemical platforms derived from cellulosic biomass.[1–3] It has been widely used as a versatile precursor for the creation of high-value fine chemicals.[4–7] Among the many derivatives of HMF,[8–10] 2,5-diformylfuran (DFF) used as a monomer plays an important role in medicine intermediates, organic conductors, and functional polymers.[11,12] HMF could be oxidized by a thermocatalytic process at high temperature and high pressure.[13,14] However, the thermocatalytic reaction is energy-intensive and often leads to safety and environmental issues.[15]

In recent years, the selective oxidation of HMF to DFF through photocatalytic technology has drawn much attention.[12,16–18] Yurdakal *et al.* first reported the application of anatase $TiO_2$ for the catalytic oxidation of HMF in water under an ultraviolet light source.[19] The majority of the organic products were DFF with a selectivity of just 10% to 25%. Wu *et al.*[20] reported the preparation of DFF by the catalytic oxidation of HMF with $Nb_2O_5$ under visible light using trifluorobenzene as the solvent, and the yield of DFF was 20%. Giannakoudakis *et al.*[9] used $MnO_2$ nanorods as a catalyst and acetonitrile as a reaction medium and achieved UV-promoted oxidation of HMF to DFF. HMF was nearly completely converted to DFF without the addition of oxidants and bases. In addition to the aforementioned metal oxides, metal sulfides can also be used as photocatalysts.[21,22] Among a variety of metal sulfides, cadmium sulfide (CdS) has garnered significant interest due to its appropriate band gap (2.4 eV) for light harvesting and appropriate conduction band edge for various catalytic reactions.[23,24] However, the photocatalytic activity of pure CdS is insufficient due to the significant recombination of carriers and intense photocorrosion.[25,26] Cocatalysts can help move electrons and holes to the surface active sites and stop charge carriers from getting back together. They could improve the speed of the reaction and the efficiency of the photocatalytic system.[27,28] Wang *et al.* reported $Ni_xS_y$ for the electrochemical oxidation of water and found that the adsorption energy of water on $Ni_xS_y$ was close to that of water on $IrO_2$, an excellent catalyst for water oxidation, even in semiconductor photocatalysis.[29] To this end, it is highly possible

---

[a] *Key Laboratory of Advanced Light Conversion Materials and Biophotonics, Department of Chemistry, Renmin University of China, Beijing 100872, China. E-mail: tcmu@ruc.edu.cn*

[b] *Beijing Key Laboratory of Lignocellulosic Chemistry, College of Materials Science and Technology, Beijing Forestry University, Beijing 100083, China. E-mail: zmxue@bjfu.edu.cn*

† Electronic supplementary information (ESI) available. See DOI: **https://doi.org/10.1039/d2gc04535d**

that $Ni_xS_y$ also plays an important role in the photocatalytic process. However, the photocatalytic oxidation of HMF to DFF by CdS using $NiS_2$ as a cocatalyst is yet to be explored.

Nanostructure synthesis by deep eutectic solvothermal procedure has the advantage of being easy to proceed and the structure and composition can be tuned by adjusting the components of solvent, one-step preparation of the sulfide avoiding the additional oxidation process, and reactants are evenly distributed at the molecular level, thus the obtained nanostructures are homogenous. Therefore, more and more works on deep eutectic solvothermal have been carried out.[30,31]

In this work, CdS nanospheres deposited with $NiS_2$ were prepared by a one-step solvothermal method. Highly selective conversion of HMF to DFF was achieved by optimizing the synthesis conditions. *In situ* electron paramagnetic resonance (EPR) trapping experiments revealed that $^{\bullet}C_6H_4O_3$ is the major intermediate radical in the oxidation of HMF. The whole photocatalytic process occurred in water at ambient conditions without using sacrificial agents or organic solvents.

# Experimental sections

### Chemicals

Polyethylene glycol 200 (PEG 200, AR), thiourea ($CH_4N_2S$, 99.0%), ethyl alcohol ($C_2H_5OH$, AR), HMF ($C_6H_6O_3$, 99.0%), DFF ($C_6H_4O_3$, 99.0%), furfural alcohol ($C_5H_6O_2$, 99.0%) and furfural ($C_5H_4O_2$, 99.0%) were purchased from Sinopharm Chemical Reagent Co., Ltd. Cadmium acetate dihydrate ($Cd(Ac)_2{\cdot}2H_2O$, AR) and nickel nitrate hexahydrate ($Ni(NO_3)_2{\cdot}6H_2O$, AR) were bought from J&K Ltd.

### Preparation of photocatalysts

Synthesis procedure for nanostructures: PEG-based deep eutectic solvent (DES) as a solvent and sulfur source was obtained based on the previous work.[32] Here, the synthesis procedure of CdS is taken as an example. At first, DES was prepared in a 2 : 1 molar ratio of PEG 200 and thiourea at 80 °C. Then, $Cd(Ac)_2{\cdot}2H_2O$ (0.01 mol) was dissolved in 40 ml of DES and stirred at 60 °C until a homogeneous solution was formed. Next, the mixture was placed into a 50 ml Teflon-lined stainless steel autoclave and kept in an oven at 120 °C for 12 h before cooling in air. The sample was obtained by centrifugal washing with deionized (DI) water and ethanol six times. Lastly, the yellow precipitate was dried in a vacuum at 60 °C for 12 h. $NiS_2$/CdS composite was prepared using the same procedure as shown in Fig. 1. The detailed procedures for the synthesis of $NiS_2$/CdS, $NiS_2$, and $NiS_2$ + CdS are given in the ESI section.†

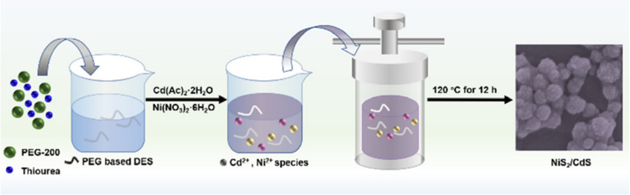

**Fig. 1** A schematic illustration of the formation of $NiS_2$/CdS photocatalyst.

### Characterization of photocatalysts

For the characterization of the obtained samples, the following techniques were used. X-ray powder diffraction (XRD) performed on a D/max-2550/PC diffractometer (Rigaku), a scanning electron microscope (SEM), energy dispersive X-ray spectroscopy (EDS), and elemental mapping images on a Hitachi SU 8010 field emission SEM combined with EDS, X-ray photoelectron spectroscopy (XPS) on an ESCALAB MK X-ray photoelectron spectrometer, morphological and microstructural features using high-resolution transmission electron microscopy (HRTEM JEOL-2010), diffuse reflectance spectroscopy using a UV-vis spectrophotometer (Hitachi U-4100), specific surface areas using the nitrogen adsorption–desorption instrument (JW-BK122 W, China), steady-state photoluminescence (PL) spectra and PL decay on an Edinburgh FLS 980 transient steady-state spectrometer, and the carbon-centered radicals by electron paramagnetic resonance (EPR, Bruker EMXnano, Bruker, Germany). Detailed procedures for the above measurements are provided in the ESI section.†

### Catalytic activity and mechanism

Experiments on photocatalytic hydrogen evolution were carried out at room temperature in hermetically sealed Pyrex glass. The produced photocatalyst powder was suspended in 50 mL of HMF aqueous solution in a typical reaction (10 mM). Before irradiation with visible light, the suspension was thoroughly degassed with $N_2$ for 30 min to completely remove dissolved oxygen. The visible light source was a 300 W Xe lamp (LabSolar II, Perfect Light Co., Ltd) equipped with a blocking filter ($\lambda \geq 420$ nm). Gaseous $H_2$ was regularly detected by a gas chromatograph (GC-2014C, Shimadzu, Japan), assembled with a TCD detector and ultrapure nitrogen as a carrier gas. The reaction solution was analyzed by HPLC, installed with a 4.6 mm × 250 mm Shim-pack GWS 5 μm C18 column, and the wavelength of the UV detector was set at 265 nm. In each measurement, 20 μL of the solution was taken out, diluted to 2 mL with an eluent, and then filtered through a 0.22 μm PTFE membrane filter. Two eluting solvents were methanol (A) and 5 mM ammonium formate aqueous solution (B), respectively. The ratio of A to B was 3 : 7 with a flow rate of 0.6 mL $\min^{-1}$ and each separation lasted for 10 min. The quantification was performed from a standard curve of known compound concentrations (Fig. S1†). The DFF yield and DFF selectivity were calculated using the following equations, respectively.

$$\text{DFF yield}(\%) = \frac{n_{\text{DFF formation}}}{n_{\text{HMF initial value}}} \times 100\% \tag{1}$$

$$\text{DFF selectivity}(\%) = \frac{n_{\text{DFF formation}}}{n_{\text{HMF consumption}}} \times 100\% \tag{2}$$

where *n* is the mole of reactant calculated from the concentration measured by HPLC.

The electrochemical experiments analysis was performed using an electrochemical workstation (Shanghai ChenHua Instrument Company). Electron paramagnetic resonance measurement (EPR) spectrometer (Bruker ELEXSYS E500). Density functional theory (DFT) calculations were carried out using the Vienna *ab initio* simulation (VASP5.4.4) code.[33] Detailed information on the above investigation is given in the ESI section.†

## Results and discussion

### Catalyst characterization

As shown in Fig. 2a, XRD patterns were used to determine the crystallization and phase purity of pure CdS NPs and $NiS_2$/CdS composites with different amounts of $NiS_2$. The major sharp peaks centered at 24.8°, 26.5°, 28.2°, 43.7°, 47.8°, 51.8° and 66.8°, correspond to the classical hexagonal CdS phase (JCPDS no. 41-1049) and show high crystallinity.[34] The successful synthesis of $NiS_2$/CdS is shown by the presence of the labeled emblematic peaks of nickel sulfide ($NiS_2$, JCPDS, no. 11-0099) in the XRD patterns after $NiS_2$ was added.[32,35]

The morphologies and internal microstructure of the catalysts were characterized by SEM and HRTEM. The well-scattered CdS spheres have a rough surface and an average diameter of around 100 nm, as seen in Fig. 2c. Pure CdS and 10% $NiS_2$/CdS had similar morphologies, with no discernible differences (as shown in Fig. S2†). While pure $NiS_2$ contained peony-like particles, its subunit sheets consisted of many ultra-thin films (Fig. 2d). Further careful observation of the HRTEM image (Fig. 2e) showed that the decoration of $NiS_2$ was successful, indicating that the interface between $NiS_2$ and CdS was tightly connected. The interplanar spacing of 0.33 nm corresponds to the (002) planes of CdS,[36] and the compact $NiS_2$ film with an interplanar spacing of 0.23 nm can be assigned to the (211) facet of $NiS_2$.[37] Elemental mapping pat-

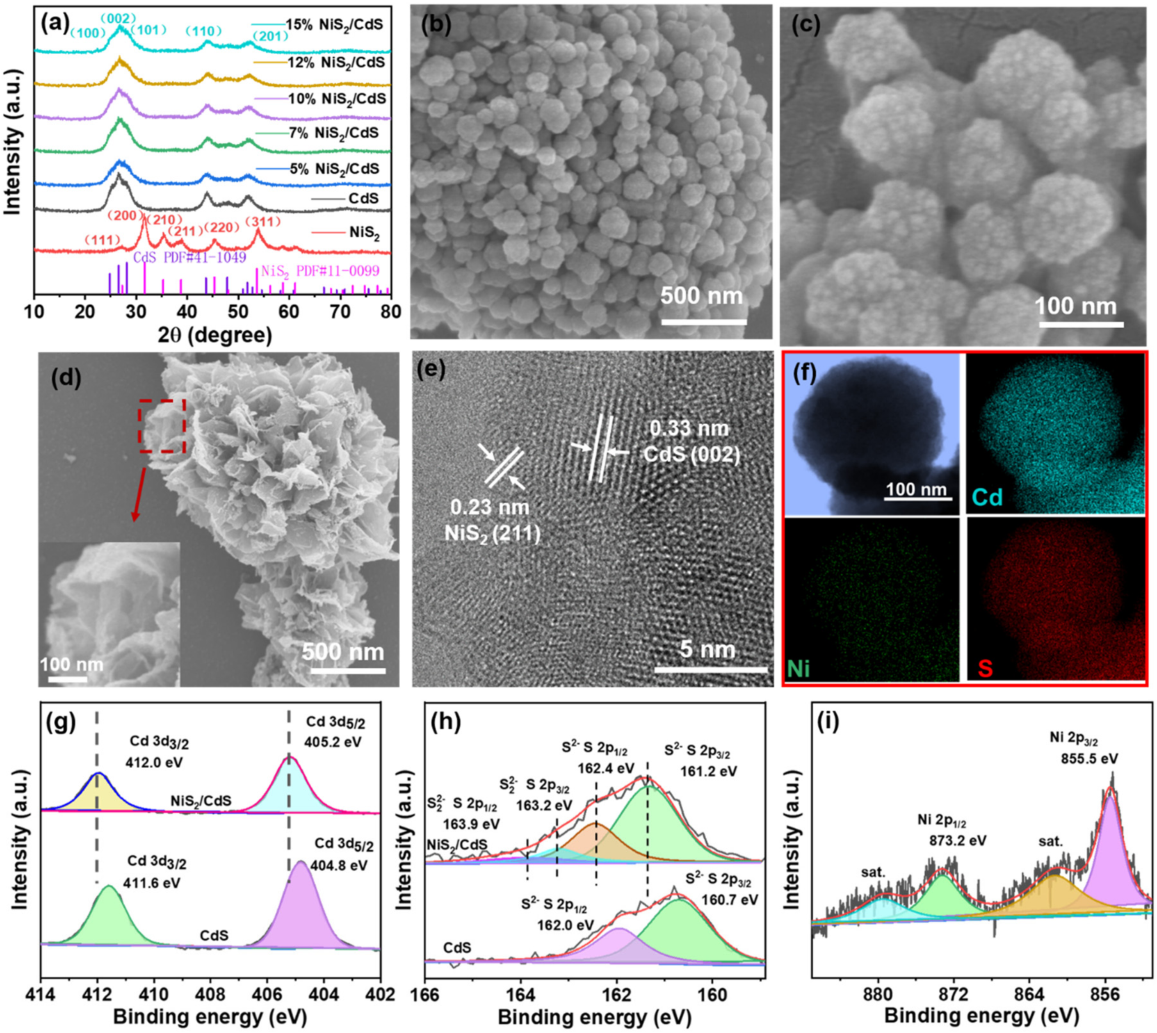

**Fig. 2** (a) XRD patterns of the as-prepared CdS, *x*% $NiS_2$/CdS, and $NiS_2$; (b and c) SEM, (e) HRTEM, (f) element mapping images of the as-prepared 10% $NiS_2$/CdS; (d) SEM of $NiS_2$; (g–i) XPS spectra for CdS and 10% $NiS_2$/CdS.

terns (Fig. 2f) clearly confirmed that Cd, Ni and S elements are uniformly distributed on the nanosphere arrays. The EDS spectrum of the 10% $NiS_2$/CdS sample is shown in Fig. S3,† further revealing that the sample had clear signals of Cd, Ni, and S elements.

X-ray photoelectron spectroscopy (XPS) study was used to learn more about the surface compositions and electronic states of $NiS_2$/CdS. The XPS measurement spectra shown in Fig. S4† indicate the presence of Cd, Ni, and S in the corresponding samples, respectively. The characteristic high-resolution XPS spectra of Cd 3d (Fig. 2g) of pure CdS and 10% $NiS_2$/CdS before the reaction exhibits two binding energy peaks at 411.6 eV, 404.8 eV, and 412.0 eV, 405.2 eV, respectively. In the S 2p spectrum of 10% $NiS_2$/CdS, the large peak starting from 159 to 165 eV can be deconvoluted into four peaks (Fig. 2h). Those with energies of 163.9 and 163.2 eV, originating from S $2p_{1/2}$ and S $2p_{3/2}$, are attributed to $S_2^{2-}$ in $NiS_2$ nanosheets, the others at 162.4 and 161.2 eV are the S $2p_{1/2}$ and S $2p_{3/2}$ of $S^{2-}$ for CdS nanospheres, respectively.[38] Significantly, the binding energies of Cd 3d characteristic peaks in $NiS_2$/CdS composite shifted slightly to higher values compared to pure CdS, implying that the density of electrons in Cd decreases after adding $NiS_2$ on CdS spheres and the existence of strong interfacial interactions between CdS nanospheres and $NiS_2$ nanosheets. In the core-level XPS spectrum of Ni 2p (Fig. 2i), the peak at about 855.5 eV is assigned to Ni $2p_{3/2}$, and the peak at 873.2 eV is assigned to Ni $2p_{1/2}$. Compared with the bare $NiS_2$ nanoparticles (the binding energy peaks of Ni $2p_{3/2}$ and Ni $2p_{1/2}$ are 855.8 eV and 873.5 eV, respectively), the binding energy of Ni was negatively shifted by 0.3 eV (Fig. S5†), indicating, a strong electronic interaction between $NiS_2$ and CdS. Two broad satellite peaks are also seen, suggesting the existence of both $Ni^{2+}$ and $Ni^{3+}$.[39]

The specific surface area and pore size distribution of the prepared samples were investigated using the $N_2$ adsorption–desorption isotherm shown in Fig. S6a,† which exhibited a typical type IV adsorption–desorption isotherm according to IUPAC with the H3 hysteresis loop at the $P/P_0$ range of 0.5–1.0.[40] Fig. S6b† shows the pore size distribution curve estimated by the Barrett–Joyner–Halender (BJH) method. These mesopores could be due to the outcome of excessive $NiS_2$ nanoparticles accumulated on the surface of CdS SPs. Moreover, $NiS_2$/CdS nanocomposites have a larger specific BET surface area than that bare CdS SPs.

## Evaluation of photocatalytic performance

The photocatalytic activities of individual CdS and $NiS_2$/CdS for the oxidation of HMF to DFF and $H_2$ (eqn (1)) were measured in water under visible light irradiation. To optimize the catalyst amount, experiments adding different amounts (10 mg, 25 mg, 50 mg, 100 mg, and 150 mg) of 10% $NiS_2$/CdS catalyst were conducted in 50 mL of HMF (10 mM) aqueous solution. As shown in Fig. S7a,† it is obvious that the lower the amount of sample added, the greater the catalytic rate per unit mass. However, when a smaller amount of materials was added, the total product per unit volume of the solution also became less for a certain period of time (Fig. S7b†), which is not conducive to industrialized production (large quantities of products cannot be obtained in a short period of time). Based on the comprehensive consideration of the amount of the catalyst used and the output per unit time per unit volume of the solution, either 25 mg or 50 mg of the catalyst in 50 mL of HMF (10 mM) in water is a good choice. Herein, we added 50 mg samples in 50 mL of HMF (10 mM) aqueous solution as the unified standard to continue the next series of research.

As illustrated in Fig. 3a, the yield rates of high value-added fine chemical DFF and $H_2$ over bare CdS are around 51.8 and 48.6 μmol $g^{-1}$ $h^{-1}$, respectively. The selectivity of DFF is about 82.0% due to the generation of trace byproducts such as 2,5-furandimethanol (DHMF) and 5-hydroxymethyl-2-furancarboxylic acid (HMFCA) (Fig. S8†).[41] Notably, the addition of $NiS_2$ considerably increases the production rates of DFF and $H_2$, showing that $NiS_2$ is an efficient way to enhance photocatalytic systems. Moreover, the production rates of DFF and $H_2$ evolution are also dependent on the amount of $NiS_2$ in $NiS_2$/CdS. The optimized amount of $NiS_2$ in $NiS_2$/CdS was 10%. DFF and $H_2$ can be produced at rates of up to 519.64 and 476.60 μmol $g^{-1}$ $h^{-1}$, respectively, which are around 10.03 and 9.81 times higher than that on bare CdS. Additionally, DFF's selectivity over 10% $NiS_2$/CdS could increase up to 90.2%. When the $NiS_2$ loading reached 12%, the generation rate decreased significantly. This is because $NiS_2$ and CdS could expose most interfaces on the surface of 10% $NiS_2$/CdS, therefore, there were most corresponding photocatalytic active sites. Intriguingly, as the proportion of $NiS_2$ increases, so does the selectivity of DFF with a maximum value of 95.2%. From

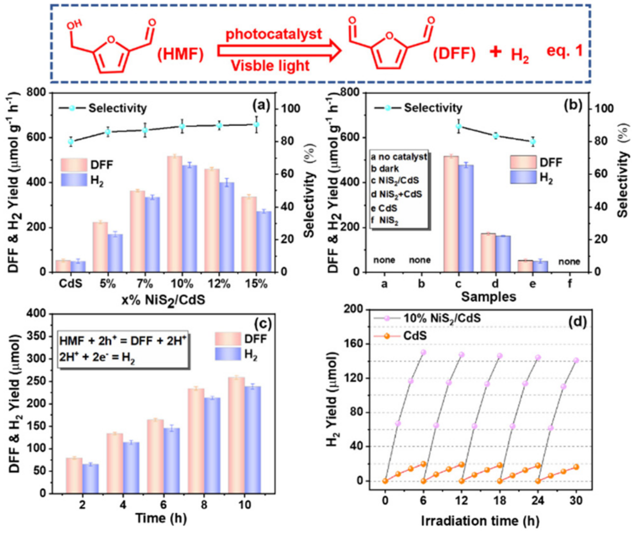

Fig. 3 (a) Photocatalytic selective transformation of HMF for DFF conversion and $H_2$ production and DFF selectivity over CdS and $x$% $NiS_2$/CdS samples; (b) comparison of CdS, $NiS_2$, 10% $NiS_2$/CdS, 10% $NiS_2$ + CdS samples and no catalyst added for the photocatalytic selective transformation of HMF; (c) time-online photocatalytic selective transformation of HMF activity over the 10% $NiS_2$/CdS sample. (d) Cyclic photocatalytic selective transformation of HMF over CdS and 10% $NiS_2$/CdS samples.

Fig. 3b, it is evident that 10% $NiS_2$ + CdS has significantly less photocatalytic activity than 10% $NiS_2$/CdS, but stronger photocatalytic activity than CdS. This indicates that $NiS_2$ is indeed an effective cocatalyst at enhancing the photocatalytic activity of CdS, and it is quite necessary to optimize the interfaces between the photocatalyst and the cocatalyst. The control studies, on the other hand, showed that DFF and $H_2$ were undetectable in the absence of photocatalysts or visible light irradiation. These findings demonstrate that: (1) the production of DFF and $H_2$ is actually activated by visible-light-driven photocatalysis; (2) $NiS_2$ as a cocatalyst could efficiently enhance the photocatalytic activity of CdS for the conversion of DFF and $H_2$; (3) the synergistic effect between $NiS_2$ and CdS is an ideal prerequisite for enhancing the photoredox activity. The reaction time was extended from 2 hours to 10 hours to examine the catalyst performance over time (Fig. 3c). No peaks for other possible products were detected, indicating the high purity of the photocatalytic biomass products (Fig. S9†). It can be seen that the photocatalytic activity of 10% $NiS_2$/CdS on the generation of DFF and $H_2$ increases gradually with the increase of the reaction time. The reactive stability of 10% $NiS_2$/CdS as a representative sample has been evaluated by examining the $H_2$ yield using the same system for photocatalytic conversion, repeatedly, five times. As shown in Fig. 3d, the decay for long-time visible-light-driven hydrogen evolution of pure CdS is larger than that of 10% $NiS_2$/CdS as a result of the known photocorrosion of metal sulfides. The binding energy changes of Cd in CdS and 10% $NiS_2$/CdS before and after the photostability test can be seen in Fig. S10.† The results show that the cocatalyst $NiS_2$ can inhibit the photocorrosion of CdS. The photostability of $NiS_2$/CdS composites is related to the effective separation of the photoexcited electrons and holes in CdS by $NiS_2$. The crystallinity (Fig. S11†) and morphology (Fig. S12†) of the material remained unchanged after irradiation, indicating that the photoreaction had no effect on the morphology and crystal morphology of the material. The crystallinity and morphology of $NiS_2$/CdS nanospheres do not change after the photoreaction, which indicates that the photoreaction did not affect the morphology and crystal form of the material. We compared the photocatalytic oxidation of HMF with those of the previously reported photocatalysts under both similar and different conditions (Table S1†). We can see that the photocatalyst in our work clearly exhibits a high photocatalytic rate and high selectivity.

Furfuryl alcohol (biomass derivative) as an analog of HMF can be converted to valuable platform chemicals through high-temperature catalysis in the solution.[42] To check the broad scope, we selected furfural alcohol for photocatalytic conversion on 10% $NiS_2$/CdS nanocrystals. Furfural alcohol (one of the biomass derivatives) has been converted to valuable platform chemicals biomass derivatives through high-temperature catalysis in the solution. The catalyst performance over time is shown in Fig. S13† (the corresponding standard curves are shown in Fig. S14†). Furfural and $H_2$ can be produced at rates of up to 611.40 and 561.86 μmol $g^{-1}$ $h^{-1}$, respectively. The selectivity of furfural was about 98.7%.

## Photocatalytic mechanism

The optical characteristics of pure CdS and its mixtures were also investigated by the UV-vis diffuse reflectance spectra. As shown in Fig. S15a,† the spectrum shifted upwards with increasing $NiS_2$ content. Similar to pure CdS nanosheets, $NiS_2$/CdS showed typical semiconducting absorption at around 520 nm. $NiS_2$ loaded on CdS nanospheres demonstrated a considerable increase in light absorption from 500 to 750 nm due to its strong light absorption ability. In addition, the loading of $NiS_2$ does not affect the light absorption edges, indicating that it does not influence the lattice of CdS. Fig. S15b† shows the band gaps of CdS, 10% $NiS_2$/CdS, and 15% $NiS_2$/CdS. Band gap energy ($E_g$) values for other samples can be found in Table S2.† The band gap energy values of CdS, 5% $NiS_2$/CdS, 7% $NiS_2$/CdS, 10% $NiS_2$/CdS, 12% $NiS_2$/CdS, and 15% $NiS_2$/CdS were 2.43 eV, 2.42 eV, 2.41 eV, 2.39 eV, 2.38 eV, and 2.37 eV, respectively. With the increasing content of $NiS_2$, the band gap energy values of the samples decrease, which indicates that the decoration of the CdS lattice with $NiS_2$ slightly decreases its band gap. The band gap energy values of the products are evaluated using the Kubelka–Munk function, and the corresponding formula is as follows:

$$(ahv)^2 = c(hv - E_g) \tag{3}$$

where $a$ and $v$ represent the absorption coefficient and frequency, respectively, $c$ and $h$ are constants.

Capacitance measurements by the Mott–Schottky equation are used to quantify electron carrier density.[43]

$$\frac{1}{C^2} = \left(\frac{2}{N_D e_0 \varepsilon \varepsilon_0}\right)\left[(E - E_{FB}) - \frac{kT}{e_0}\right] \tag{4}$$

where $C$ is the space charge capacity of the semiconductor, $N_D$ refers to the electron carrier density, $\varepsilon_0$ and $\varepsilon$ are set as the permittivity of a vacuum and the relative permittivity of the semiconductor, $E$, $e_0$, $E_{FB}$, $k$, and $T$ are the applied potential, elemental charge value, flat band potential, Boltzmann constant, and temperature, respectively. As shown in Fig. S16,† the slope of the Mott–Schottky plots and n-type characteristics of both pure CdS and 10% $NiS_2$/CdS can be obtained. The experimentally determined flat–band potentials ($E_{FB}$) of bare CdS and 10% $NiS_2$/CdS are −0.71 V and −0.63 V (*vs.* Ag/AgCl), respectively. Assuming that $E_{FB}$ is equivalent to the conduction band ($E_{CB}$) position, the band gap energy $E_g$ of CdS and 10% $NiS_2$/CdS are 2.43 eV and 2.39 eV, respectively. According to the formula $E_g = E_{VB} - E_{CB}$, the valence band edge potentials for bare CdS and 10% $NiS_2$/CdS is 1.72 V and 1.76 V, respectively. For the conversion of HMF into DFF, the potential of HMF to DFF ($E_{HMF/DFF}$) and the potential of DFF to oxidized DFF ($E_{DFF/oxidized\ DFF}$) are 1.61 V and 2.03 V, respectively.[44] The VB of CdS is exactly halfway between these two potentials, resulting in the major product of DFF (Scheme 1).

The charge transfer mechanism at the $NiS_2$/CdS interface was investigated using the density functional theory (DFT). The theoretical work functions ($\Phi$) of CdS (Fig. 4a) and $NiS_2$ (Fig. 4b) were calculated to be 6.46 and 8.76 eV, respectively,

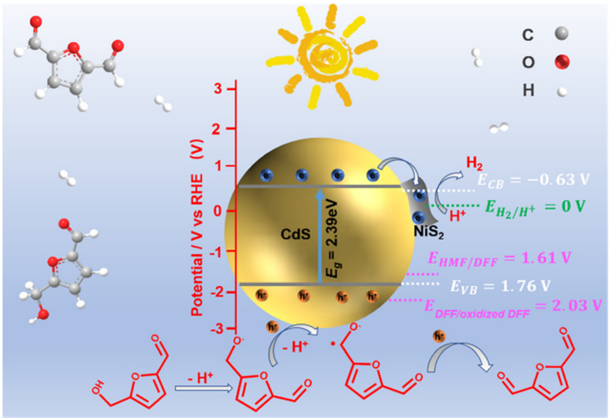

**Scheme 1** Schematic illustration of the determined CB and VB edges of $NiS_2/CdS$ and oxidizing potential.

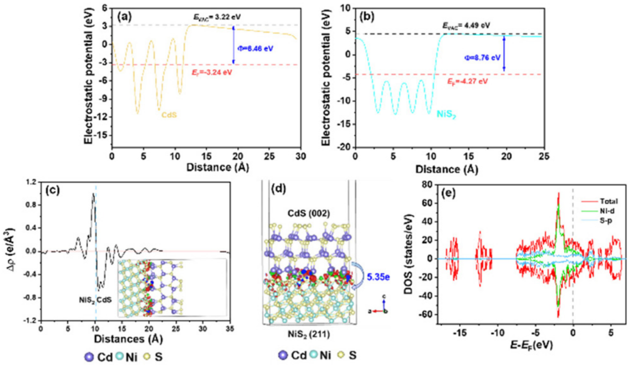

**Fig. 4** Theoretical work functions of CdS (a) and $NiS_2$ (b). (c) Electron density difference (e Å$^{-3}$) and (d) Bader electron transfer at the $NiS_2/CdS$ interfaces. (e) The density of states of $NiS_2$.

indicating that the electrons are prone to gather on $NiS_2$. The deformation charge density (Fig. 4c) shows that electrons tend to transfer from CdS to $NiS_2$ at the $NiS_2/CdS$ interface. Therefore, the S atoms in $NiS_2$ primarily facilitated the gain of electrons. Specifically, the Bader charge shows that the electron transport from CdS to $NiS_2$ is 5.35*e* (Fig. 4d). The electron transfer route is consistent with the binding energy shifts of S 2p and the obtained work function above.

According to the aforementioned findings, a possible catalytic mechanism for the photocatalytic conversion of HMF into DFF along with $H_2$ evolution on $NiS_2/CdS$ nanospheres is proposed (Scheme 2). $NiS_2$ has metallic properties and high electrical conductivity. The density of states also confirmed the metallic nature of $NiS_2$ (Fig. 4e). An interfacial barrier area, also known as a barrier layer, forms at the contact interfaces of $NiS_2$ and CdS when they are in close proximity. Due to the lower Fermi level ($E_F$ $NiS_2$) compared to that of CdS ($E_F$ CdS) and surface metallic characteristics, the photogenerated electrons from CdS can quickly move to $NiS_2$, and the recombination of photogenerated electron–hole pairs is prevented. Additionally, $NiS_2$ can easily mix with surface-adsorbed $H_2O$ to generate Ni–H bonds in addition to serving as active sites for the hydrogen evolution reaction. The electrons on $H_2O$-bonded $NiS_2$ will generate $H_2$ with adsorbed $H^+$, which further enhances the photocatalytic performance and the $NiS_2/CdS$ nanohybrid system stability. The photoexcited electrons travel to the CB of the primary catalyst CdS under visible light, while an equivalent number of photoexcited holes are left on the VB of CdS. The cocatalyst $NiS_2$ receives the electrons quickly delivered from the CB of CdS. In order to convert HMF into DFF, photoexcited holes on CdS first activate the alkoxide anion that was deprotonated from HMF, resulting in the formation of appropriate carbon radicals and the release of an $H^+$ ion. The generated carbon radicals then continue to react with the holes to create DFF molecules. One HMF molecule can produce two $H^+$ ions in total, which can combine with two electrons on $NiS_2$. Therefore, the two isolated reactions can be successfully carried out without the use of any sacrificial agents, and aqueous solution green recycling can be developed.

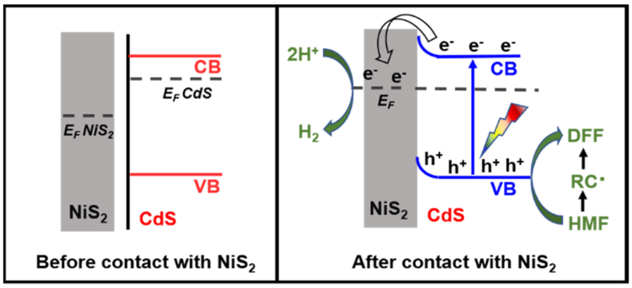

**Scheme 2** Energy band diagrams of the pure CdS and $NiS_2/CdS$ before contact with metallic $NiS_2$ and the interfacial photoinduced charge transfer and reaction after contact with $NiS_2$ and light irradiation.

### Photoluminescence (PL) spectra and photoelectric properties

To further investigate the effect of the deposited $NiS_2$ in separating the internal carriers on the photocatalytic coproduction of $H_2$ and DFF, the PL spectra of pure CdS and 10% $NiS_2/CdS$ were measured. The PL emission intensity was clearly quenched when the $NiS_2$ was modified on CdS (Fig. 5a). The time-resolved PL (TRPL) decay spectra were also recorded to explore the carrier transfer dynamics, as shown in Fig. 5b. The decay curves of the produced samples match the following double exponential equation quite well:

$$I_{(t)} = I_0 + A_1 \exp\left(\frac{-t}{\tau_1}\right) + A_2 \exp\left(\frac{-t}{\tau_2}\right) \tag{5}$$

where $I_0$ is the baseline correction value; $A_1$ and $A_2$ are the prefactors, respectively; $\tau_1$ and $\tau_2$ are the lifetimes (ns) of the radiative and nonradiative recombination processes, respectively.[45] The calculation formula of the average life ($\tau_{ave}$) is as follows:

$$\tau_{ave} = (A_1{\tau_1}^2 + A_2{\tau_2}^2)/(A_1\tau_1 + A_2\tau_2) \tag{6}$$

The double-exponential fitting results are summarized in Table S3.† A significant PL quenching and lifespan enhance-

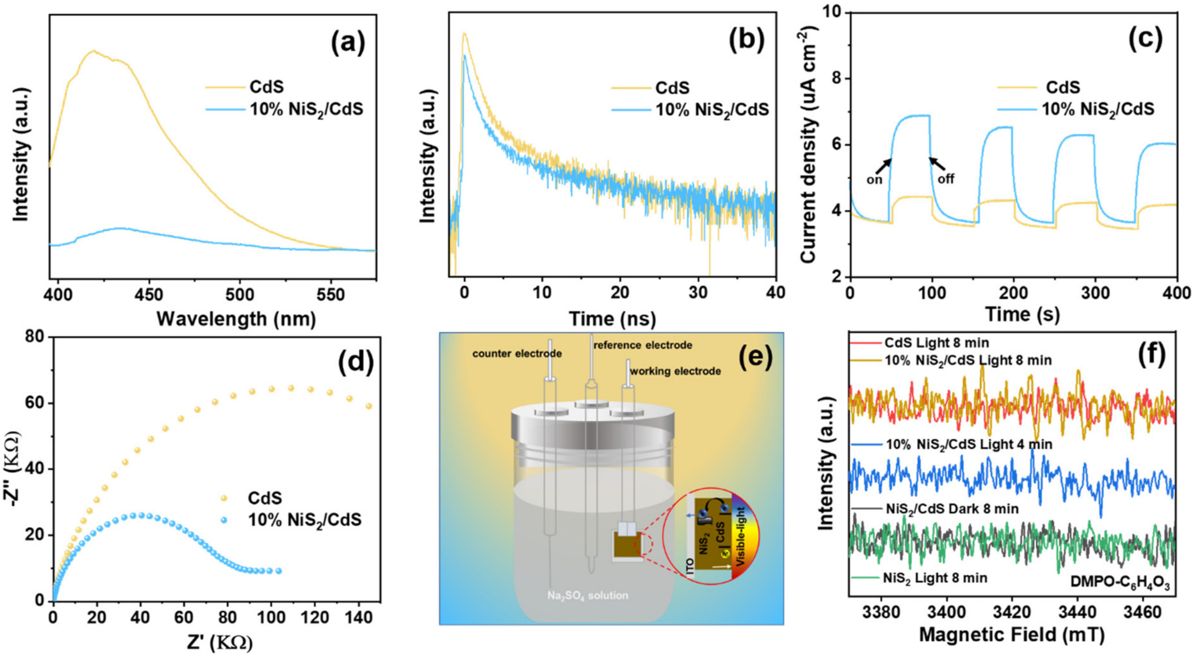

**Fig. 5** (a) PL spectra, (b) TRPL decay spectra, (c) transient photocurrent responses, and (d) EIS spectra for pure CdS and 10% $NiS_2$/CdS; (e) schematic of photochemical cell and electron flow; (f) *in situ* EPR spectra for CdS, $NiS_2$ and 10% $NiS_2$/CdS in a mixture solution of HMF in the presence of spin-trapping agent DMPO with or without visible light irritation.

ment suggested that carrier transfer and separation in $NiS_2$/CdS were significantly more efficient.[46] Photoelectrochemical tests were also carried out to further examine the separation and transfer ability of the charges. The transient photocurrent responses of the two samples exposed to visible light (420 nm) with regular on/off cycles are depicted in Fig. 5c. It is evident that the 10% $NiS_2$/CdS sample displayed much greater photocurrent density than that of CdS, implying a more efficient carrier separation in 10% $NiS_2$/CdS.[47] Moreover, the electrochemical impedance spectroscopy (EIS) Nyquist plot of 10% $NiS_2$/CdS exhibited a smaller arc radius than pure CdS (Fig. 5d), which suggested that there was a lower interface charge transfer resistance in 10% $NiS_2$/CdS.

Fig. S17† shows the LSV polarization curves of pristine CdS, $NiS_2$, and 10% $NiS_2$/CdS at a scan rate of 5 mV $s^{-1}$. It is clear to see that the electrocatalytic activity is $NiS_2$ > 10% $NiS_2$/CdS > CdS. This indicates that $NiS_2$ can effectively accelerate the electrocatalytic hydrogen evolution kinetics of nanocomposites, thereby, greatly improving the HER (hydrogen evolution reaction) performance of nanocomposites.[48] The corresponding schematic of the photochemical cell and electron flow is shown in Fig. 5e. Nevertheless, all of the above results prove that the $NiS_2$/CdS nanosphere structure could accelerate the photogenerated carrier separation, thus improving the photocatalytic performance.

### Electron paramagnetic resonance study

*In situ* EPR studies were performed to detect reactive intermediates during the catalytic reactions and understand the photocatalytic dehydrogenation process of HMF in prepared composites. As illustrated in Fig. 5f, no EPR signals could be seen on the blank tests (performed in the dark or under visible light irradiation with bare $NiS_2$). But after irradiation, signals corresponding to the peaks of carbon-centered radicals were clearly seen across both pure CdS and 10% $NiS_2$/CdS. The intensity of the signals increased with the radiation time, indicating the formation of carbon-centered radicals over 10% $NiS_2$/CdS during the photocatalytic reaction.[49] Moreover, the intensity of 10% $NiS_2$/CdS is clearly stronger than that of CdS, showing that more carbon-centered radicals are produced over 10% $NiS_2$/CdS. The results are consistent with the above photocatalytic activity.

## Conclusions

In this study, $NiS_2$/CdS was synthesized *via* a one-step deep eutectic solvothermal procedure. The obtained $NiS_2$/CdS composites, especially 10% $NiS_2$/CdS nanospheres, can be used as a highly effective, bifunctional photocatalyst for the selective conversion of biomass-derived alcohols to high-value-added fine chemical DFF and clean energy ($H_2$) without adding the sacrificial agent. DFF and $H_2$ can be produced at rates of up to 519.64 and 476.60 μmol $g^{-1}$ $h^{-1}$, which are about 10.03 and 9.81 times larger, respectively, than that on bare CdS under visible light irradiation. The DFF selectivity of $x$% $NiS_2$/CdS can reach up to 95.2%. Photocurrent, EIS, LSV, PL, and TRPL experiments and DFT calculations clearly showed that $NiS_2$ can effectively facilitate the separation and migration of photoexcited charges when used as a co-catalyst. A rational photocatalytic process was proposed on the basis of UV–vis, Mott–Schottky, and EPR. Importantly, this work offers a promising method for creating innovative, non-precious metal, and efficient visible-light-driven composite photocatalysts. The photocatalytic dehydrogenation strategy could be used in other organic transformation processes.

## Conflicts of interest

There are no conflicts to declare.

## Acknowledgements

This work has been funded by the National Natural Science Fund of China (No. 22073112, 22238011).

## Notes and references

1 S. Xu, P. Zhou, Z. Zhang, C. Yang, B. Zhang, K. Deng, S. Bottle and H. Zhu, *J. Am. Chem. Soc.*, 2017, **139**, 14775–14782.

2 T. Chhabra, P. Dwivedi and V. Krishnan, *Green Chem.*, 2022, **24**, 898–910.

3 T. Chhabra, A. Bahuguna, S. S. Dhankhar, C. M. Nagaraja and V. Krishnan, *Green Chem.*, 2019, **21**, 6012–6026.

4 C. Xu, E. Paone, D. Rodriguez-Padron, R. Luque and F. Mauriello, *Chem. Soc. Rev.*, 2020, **49**, 4273–4306.

5 Y. C. Yang and T. C. Mu, *Green Chem.*, 2021, **23**, 4228–4254.

6 T. Wang, L. Tao, X. Zhu, C. Chen, W. Chen, S. Du, Y. Zhou, B. Zhou, D. Wang, C. Xie, P. Long, W. Li, Y. Wang, R. Chen, Y. Zou, X.-Z. Fu, Y. Li, X. Duan and S. Wang, *Nat. Catal.*, 2022, **5**, 66–73.

7 K. Gu, D. Wang, C. Xie, T. Wang, G. Huang, Y. Liu, Y. Zou, L. Tao and S. Wang, *Angew. Chem., Int. Ed.*, 2021, **60**, 20253–20258.

8 C. Li, J. Li, L. Qin, P. Yang and D. G. Vlachos, *ACS Catal.*, 2021, **11**, 11336–11359.

9 D. A. Giannakoudakis, V. Nair, A. Khan, E. A. Deliyanni, J. C. Colmenares and K. S. Triantafyllidis, *Appl. Catal., B*, 2019, **256**, 117803.

10 A. Khan, M. Goepel, A. Kubas, D. Lomot, W. Lisowski, D. Lisovytskiy, A. Nowicka, J. C. Colmenares and R. Glaser, *ChemSusChem*, 2021, **14**, 1351–1362.

11 Z. H. Zhang and K. J. Deng, *ACS Catal.*, 2015, **5**, 6529–6544.

12 M. Zhang, Z. Li, X. Xin, J. Zhang, Y. Feng and H. Lv, *ACS Catal.*, 2020, **10**, 14793–14800.

13 X. Huang, O. Akdim, M. Douthwaite, K. Wang, L. Zhao, R. J. Lewis, S. Pattisson, I. T. Daniel, P. J. Miedziak, G. Shaw, D. J. Morgan, S. M. Althahban, T. E. Davies, Q. He, F. Wang, J. Fu, D. Bethell, S. McIntosh, C. J. Kiely and G. J. Hutchings, *Nature*, 2022, **603**, 271–275.

14 E. Hayashi, Y. Yamaguchi, K. Kamata, N. Tsunoda, Y. Kumagai, F. Oba and M. Hara, *J. Am. Chem. Soc.*, 2019, **141**, 890–900.

15 L. Hu, A. Y. He, X. Y. Liu, J. Xia, J. X. Xu, S. Y. Zhou and J. M. Xu, *ACS Sustainable Chem. Eng.*, 2018, **6**, 15915–15935.

16 X. Wu, N. Luo, S. Xie, H. Zhang, Q. Zhang, F. Wang and Y. Wang, *Chem. Soc. Rev.*, 2020, **49**, 6198–6223.

17 T. Chhabra, S. Dhingra, C. M. Nagaraja and V. Krishnan, *Carbon*, 2021, **183**, 984–998.

18 S. Dhingra, T. Chhabra, V. Krishnan and C. M. Nagaraja, *ACS Appl. Energy Mater.*, 2020, **3**, 7138–7148.

19 S. Yurdakal, B. S. Tek, O. Alagoz, V. Augugliaro, V. Loddo, G. Palmisano and L. Palmisano, *ACS Sustainable Chem. Eng.*, 2013, **1**, 456–461.

20 H. Zhang, Q. Wu, C. Guo, Y. Wu and T. Wu, *ACS Sustainable Chem. Eng.*, 2017, **5**, 3517–3523.

21 M. D. Regulacio and M. Y. Han, *Acc. Chem. Res.*, 2016, **49**, 511–519.

22 P. Zhang, S. B. Wang, B. Y. Guan and X. W. Lou, *Energy Environ. Sci.*, 2019, **12**, 164–168.

23 X. Wu, S. Xie, H. Zhang, Q. Zhang, B. F. Sels and Y. Wang, *Adv. Mater.*, 2021, **33**, 2007129.

24 S. Dhingra, M. Sharma, V. Krishnan and C. M. Nagaraja, *J. Colloid Interface Sci.*, 2022, **608**, 1040–1050.

25 Y. Zhong, G. Zhao, F. Ma, Y. Wu and X. Hao, *Appl. Catal., B*, 2016, **199**, 466–472.

26 X.-j. Wang, X.-l. Li, C. Liu, F.-t. Li, Y.-p. Li, J. Zhao, R.-h. Liu and G.-d. Li, *Int. J. Hydrogen Energy*, 2018, **43**, 219–228.

27 B. He, C. Bie, X. Fei, B. Cheng, J. Yu, W. Ho, A. A. Al-Ghamdi and S. Wageh, *Appl. Catal., B*, 2021, **288**, 119994.

28 Z. Dou, Z. Zhang, H. Zhou and M. Wang, *Angew. Chem., Int. Ed.*, 2021, **60**, 16399–16403.

29 Y. Wang, Z. Fang, Q. Dong, Y. Chu, X. Shi, M. Song and Z. Hao, *Appl. Surf. Sci.*, 2019, **491**, 590–594.

30 D. Yu, Z. Xue and T. Mu, *Cell Rep. Phys. Sci.*, 2022, 100809.

31 D. Yu, Z. Xue and T. Mu, *Chem. Soc. Rev.*, 2021, **50**, 9345–9345.

32 X. Zhao, X. Lan, D. Yu, H. Fu, Z. Liu and T. Mu, *Chem. Commun.*, 2018, **54**, 13010–13013.

33 G. Kresse and J. Furthmuller, *Phys. Rev. B: Condens. Matter Mater. Phys.*, 1996, **54**, 11169–11186.

34 J. Yuan, J. Wen, Y. Zhong, X. Li, Y. Fang, S. Zhang and W. Liu, *J. Mater. Chem. A*, 2015, **3**, 18244–18255.

35 J. Yue, J. Xu, J. Niu and M. Chen, *Int. J. Hydrogen Energy*, 2019, **44**, 19603–19613.

36 J. Zou, W. Zhou, L. Huang, B. Guo, C. Yang, Y. Hou, J. Zhang and L. Wu, *J. Catal.*, 2021, **400**, 347–354.

37 B. Zhang, H. Fu and T. Mu, *Green Chem.*, 2022, **24**, 877–884.

38 J. Zou, W. Zhou, L. Huang, B. Guo, C. Yang, Y. Hou, J. Zhang and L. Wu, *J. Catal.*, 2021, **400**, 347–354.

39 J. Liang, Y. Wang, Q. Liu, Y. Luo, T. Li, H. Zhao, S. Lu, F. Zhang, A. M. Asiri, F. Liu, D. Ma and X. Sun, *J. Mater. Chem. A*, 2021, **9**, 6117–6122.

40 K. S. W. Sing, *Pure Appl. Chem.*, 1985, **57**, 603–619.

41 S. Dhingra, M. Sharma, V. Krishnan and C. M. Nagaraja, *J. Colloid Interface Sci.*, 2022, **615**, 346–356.

42 T. Chhabra, J. Rohilla and V. Krishnan, *Mol. Catal.*, 2022, **519**, 112135.

43 L. Shi, W. Zhou, Z. Li, S. Koul, A. Kushima and Y. Yang, *ACS Nano*, 2018, **12**, 6335–6342.

44 S. Meng, H. Wu, Y. Cui, X. Zheng, H. Wang, S. Chen, Y. Wang and X. Fu, *Appl. Catal., B*, 2020, **266**, 118617.

45 X. W. Shi, S. Kim, M. Fujitsuka and T. Majima, *Appl. Catal., B*, 2019, **254**, 594–600.

46 X. L. Bao, H. L. Li, Z. Y. Wang, F. X. Tong, M. Liu, Z. K. Zheng, P. Wang, H. F. Cheng, Y. Y. Liu, Y. Dai, Y. C. Fan, Z. Y. Li and B. B. Huang, *Appl. Catal., B*, 2021, **286**, 119885.

47 M. Liu, L. R. Zheng, X. L. Bao, Z. Y. Wang, P. Wang, Y. Y. Liu, H. F. Cheng, Y. Dai, B. B. Huang and Z. K. Zheng, *Chem. Eng. J.*, 2021, **405**, 126654.

48 C. Li, H. Wang, S. B. Naghadeh, J. Z. Zhang and P. Fang, *Appl. Catal., B*, 2018, **227**, 229–239.

49 X. Bao, M. Liu, Z. Wang, D. Dai, P. Wang, H. Cheng, Y. Liu, Z. Zheng, Y. Dai and B. Huang, *ACS Catal.*, 2022, **12**, 1919–1929.